Geophysical, remote sensing, GIS, and isotopic applications for a better understanding of the structural controls on groundwater flow in the Mojave Desert, California

D. Dailey [a], W. Sauck [a], M. Sultan [a,*], A. Milewski [b], M. Ahmed [a,c], W.R. Laton [d], R. Elkadiri [a], J. Foster [d], C. Schmidt [a], T. Al Harbi [a,e]

[a] Department of Geosciences, Western Michigan University, Kalamazoo, MI 49008, USA
[b] Department of Geology, University of Georgia, Athens, GA 30602, USA
[c] Department of Geology, Faculty of Science, Suez Canal University, Ismailia 41522, Egypt
[d] Department of Geology, California State University Fullerton, Fullerton, CA 92834, USA
[e] Department of Geology and Geophysics, King Saud University, Riyadh 11451, Saudi Arabia

ARTICLE INFO

ABSTRACT

Study region: Mojave Desert, USA.
Study focus: An integrated (near-surface geophysics, remote sensing, isotopic analyses) study was conducted in the Mojave River Basin and Morongo Groundwater Basin to investigate potential effects that the Helendale Fault [HF] and basement uplifts might have on groundwater flow in the Mojave Desert.
New hydrological insights for the region: The HF traces were mapped using LiDAR and Geoeye-1 imagery (surface) and magnetic profiles (subsurface). Shallow basement parallel to and west of the HF was detected using the Vertical Electrical Soundings (VESs). Conductive water-saturated breccia was detected along the HF using the Very Low Frequency (VLF) electromagnetic measurements. Isotopic analyses (δD and δ^{18}O) for groundwater samples from productive shallow wells, and springs sampled west of the HF and the basement uplift are less depleted (Group I: Fifteenmile Valley Groundwater sub-basin [FVGS]; average δD: −86.8‰; δ^{18}O: −11.8‰) than samples east of the basement uplift (Group II: Lucerne Valley Groundwater sub-basin [LVGS]; average δD: −95.0‰; δ^{18}O: −12.1‰), whereas samples proximal to, the fault have compositions similar to Group I but show evidence for mixing with Group II compositions (Group III; average δD: −88.8‰; δ^{18}O: −11.5‰). Findings are consistent with the HF channeling groundwater from the San Bernardino Mountains with basement uplifts acting as barriers to lateral groundwater flow and could be applicable to similar settings across the Mojave Desert and elsewhere worldwide.

* Corresponding author at: Department of Geosciences, Western Michigan University, 1903 West Michigan Avenue, Kalamazoo, MI 49008, USA. Tel.: +1 269 387 5487/5451; fax: +1 269 387 5513.
   E-mail address: mohamed.sultan@wmich.edu (M. Sultan).

1. Introduction

The structural controls on groundwater accumulation and flow exhibit a wide range of variability. Faults can act as highly permeable pathways, or as barriers for groundwater flow depending on the aquifer lithology, aquifer hydrologic conditions, and fault characteristics (Bense and Person, 2006; Celico et al., 2006; Dewandel et al., 2006). The extent to which groundwater flows along the strike of a fault is controlled by fault properties (e.g., width of core and deformation zones, parent material), hydrologic framework (e.g., permeability of the individual fault rocks/fractures, geometric architecture in three dimensions, extent of clay core), and hydrologic parameters (e.g., fault specific resistance, transmissibility, hydraulic head) (Bense et al., 2003; Lunn et al., 2008; Caine and Minor, 2009; Faulkner et al., 2010). Various mechanisms were suggested to explain the damming effect of the fault zones across unconsolidated sediments including the cementation or mineralization of the fault zone, grain crushing and grain realignment and juxtaposition seals (Bense and Person, 2006; Knipe, 1993). In this study we adopt an integrated (geophysics, remote sensing, GIS, and isotopic analyses) approach to investigate the potential role of structural elements, faults and basement uplifts, in controlling the groundwater flow in the Mojave Desert.

The Mojave Desert occupies areas in southeastern and central California, southern Nevada, southwestern Utah, and northwestern Arizona in the United States (Fig. 1 inset). The rapidly growing population (1980 population: 64,685; 2010 population: 349,730), low humidity, high summer temperature, and the paucity of precipitation (100–140 mm/year; Londquist and Martin, 1991) in the Mojave Desert has created an ever-increasing need for freshwater resources. Surface water is limited to ephemeral flow during winter and spring storm periods.

Two main groundwater basins were recognized in the southwestern parts of the Mojave Desert, the Mojave River Groundwater Basin (MRGB), and the Morongo Groundwater Basin (MGB) (Fig. 1). Runoff and groundwater flow from the melting of snowpack over the adjacent San Bernardino Mountains constitute the principal sources of groundwater in the southern parts of the MRGB and MGB (Stamos et al., 2003; USGS, 2004), whereas the northern and central portions of the basin are largely recharged by groundwater and surface flow from surrounding mountain ranges such as the Cougar Buttes and Granite Mountains (Fig. 1), as well as infiltration via the Mojave River floodplain aquifer.

Increasing extraction of groundwater from the MRGB and the MRB has affected various sections in the basin to varying degrees. The central portions of the MRGB witnessed a progressive decline in water levels over the years (20 m from 1950 to 1986), whereas areas proximal to the mountains showed minimal or significantly less decline (Smith and Pimentel, 1998). One popular explanation for the groundwater deficits in the central parts of the basin is that the dextral faults in the area acted as barriers for lateral (across-fault) flow of groundwater from the mountains toward the central parts of the basin. A better understanding of how regional and local fault systems interact with the principle aquifers in the Mojave Desert is of key importance in meeting the rising demand for groundwater resources.

In this study, we examine the role of one of the major dextral faults in the MRGB and the MRB, the Helendale Fault (HF), and its subsequent splays as potential barriers (across strike) to groundwater flow or as enhanced groundwater flow pathways along its strike that probably feed both basins. The former widely accepted hypothesis is largely based on the observed water level differences (~40 m) across the HF in the Central Lucerne Valley area and those (3–9 m) across both the Johnson Valley Fault and the Emerson Fault (Lewis, 1972; Trayler and Koczot, 1995; GSI, 2000). This explanation is at odds with reported findings elsewhere that suggest that fractured fault planes often act as enhanced groundwater flow directions along strike (e.g., Barton et al., 1995; Caine et al., 1996; Gudmundsson, 2001; Sultan et al., 2007). If such models were applicable to the HF, it could be channeling groundwater from the San Bernardino Mountains in the south to the lowlands of the MRGB and MGB in the north.

An integrated approach utilizing remote sensing (LiDAR and GEOEye-1 images), geophysical (Very Low Frequency [VLF], magnetic, and Vertical Electrical Soundings [VES]) data, isotopic (O, H stable isotope) compositions for groundwater samples, and subsurface well data was adopted to investigate (1) the potential role of the HF as a barrier for lateral groundwater flow or as an enhanced groundwater flow pathway along its strike, and (2) the distribution and nature of barriers for lateral groundwater flow in the study area. Specifically, we investigate a previously unrecognized preferential groundwater
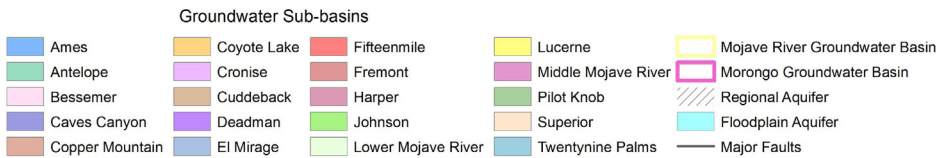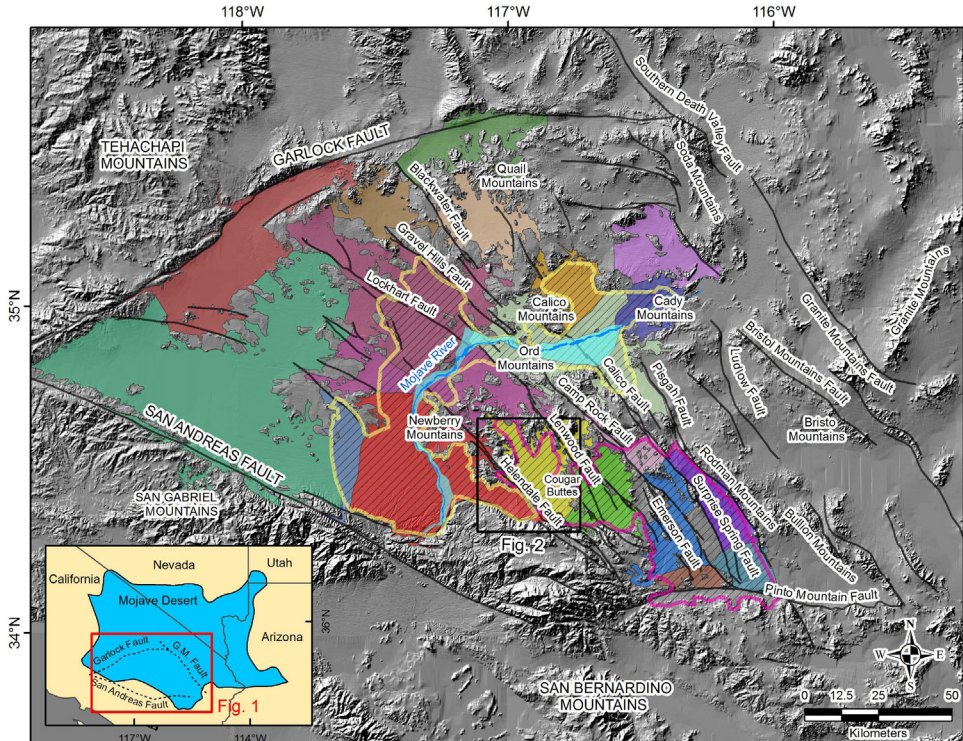
Fig. 1. Overview of the southern Mojave Desert, with hillshade applied to accentuate topographic features showing the distribution of major (1) faults (e.g., Helendale, San Andreas); (2) mountain ranges (e.g., Tehachapi, San Bernardino); (3) groundwater basins (e.g., Mojave River, Morongo); (4) groundwater sub-basins (e.g., Lucerne Valley, Fifteenmile Valley); and (5) aquifers (e.g., Regional, Floodplain). Enlargements of the study area are shown in Fig. 2A and B. The inset (lower left corner) shows the areal extent of the Mojave Desert in California, Nevada, Utah, and Arizona. Areas covered by Figs. 1 and 2 are outlined by boxes in the inset and in Fig. 1, respectively.

flow path from mountainous source areas that could be providing additional contributions to the aquifers in the study area. Specifically, we investigate the potential role of the strike-slip faults in the basin as enhanced groundwater flow pathways along strike that could provide recharge to both local and regional aquifers. We also investigate the previously-unrecognized role of basement uplifts (ridges) in controlling lateral groundwater flow in the study area. The wide distribution of similar structural elements (e.g., strike-slip faults) and landforms (mountainous areas and inland basins) throughout the MRGB, MGB, and large sectors of the Mojave Desert makes it likely that our findings could be applicable to many other similar surrounding areas.

2. Geologic and hydrogeologic setting

The southwestern Mojave Desert is characterized by the numerous mountain ranges within it, including the Tehachapi, San Bernardino, Bullion, Quail, Soda, and Calico ranges, which are separated by valleys and inland basins (Fig. 1). These mountain ranges and valleys are part of the Basin and Range

province, an area undergoing crustal thinning, pull-apart basin tectonics, and lateral displacements across the numerous dextral faults (e.g., Helendale, Lenwood, Lockhart, and Camp Rock) related to the Late Cenozoic tectonics in the area (Dokka, 1983; Dokka and Travis, 1990). These dextral fault systems formed secondarily to the San Andreas Fault, primarily as a result of extension and rotation of the Mojave Fault Block (Dokka and Travis, 1990; Dokka and Macaluso, 2001).

The MRGB (area: 3630 km^2) is bounded by the San Bernardino and San Gabriel Mountains in the south, by the Lucerne Valley to the east, and by the Antelope Valley to the west (Fig. 1). The MGB (area: 2600 km^2) is surrounded by the Ord and Granite mountains to the north, the Bullion Mountains to the east, the San Bernardino Mountains to the southwest, and the Little San Bernardino Mountains to the south (Fig. 1). Bedrock units throughout the MRGB and MGB consist mainly of Mesozoic granites and gabbros, with sparse dispersions of Tertiary volcanic units in the central and northern portions of the basin. Quaternary alluvial sediments make up the majority of surface sediments, with additional marine and non-marine sand deposits spread sparsely throughout the basin, generally near the desert playas (Fig. 2A).

Both the MRGB and MGB are characterized by a series of Cenozoic, parallel, northwest-trending dextral strike-slip faults that make up the Mojave Desert Fault Block in the eastern California Shear Zone. Their occurrence spans from the San Andreas Fault in the west to the Johnson Valley and Granite Mountains faults in the east (Fig. 1). The fault system is commonly thought of as a simple shear system with dextral faults terminating against the cross-cutting Garlock Fault to the north and the San Bernardino thrust belt in the south (Garfunkel, 1974). This model is contested by more recent research that suggests a more complex rotational system, with the majority of offset along the faults being attributable to extensional and rotational elements due to movement along the San Andreas Fault (Dokka, 1986; Dokka and Travis, 1990). The Northeast Mojave Block, located in the northeastern portion of the Mojave Desert, is a separate rotational block of dextral faults, oriented west to east and trending nearly perpendicular to the majority of the other dextral faults in the shear zone (Dokka et al., 1991).

MRGB and MGB are broken up into a series of smaller sub-basins. These sub-basins are apparently separated by ridges defined by basement and/or bedrock outcrops and shallow bedrock saddles between the exposed ridges that are proximal and parallel to the dextral fault systems in the valley. The faults originate and/or terminate against the northern and southern mountain ranges. One such sub-basin of the MGB is the Lucerne Valley Groundwater sub-basin (LVGS), a land-locked basin with limited external surface water flowing out of it (Meisling, 1984); another is the Fifteenmile Valley Groundwater sub-basin (FVGS), also called the "Upper Mojave River Valley Groundwater sub-basin" within the MRGB (Fig. 1). Fig. 2A and B reveal that the LVGS and the FVGS are separated by a northwest-southeast trending ridge that runs parallel and proximal to the HF (Fig. 1). The latter originates in the south along the San Bernardino mountain front and extends northwest across the LVGS, terminating in the Newberry Mountains. Across some of these ridges and proximal to sub-parallel faults, large differences in water levels were reported (Lewis, 1972; MWA, 2007; Trayler and Koczot, 1995; GSI, 2000). Water levels are not the only features that vary across these topographic ridges and faults. Varying groundwater flow directions were reported from aquifers separated by these topographic highs and faults, as seen in Fig. 2B.

Within the MRGB, an unconsolidated alluvial aquifer, the Floodplain Aquifer, extends along the Mojave River and is surrounded and underlain by an extensive aquifer known as the Regional Aquifer (Fig. 1). These aquifers are the primary sources of groundwater for the residents of Lucerne Valley. The interconnected alluvial basins and topographically closed basins of the Regional Aquifer extend across the entire MRGB and MGB (Izbicki, 2004). The aquifer is formed of unconsolidated older (Pleistocene to Pliocene) alluvium of the ancestral Mojave River and undifferentiated alluvium of Holocene to Pliocene age (Stamos et al., 2001).

3. Methodology

We adopted a four-step methodology. First, we collected and processed available satellite and airborne light detection and ranging (LiDAR) images to better delineate the fault traces because many of them are obscured by alluvium or too subtle to observe in the field. Also, the fine-scale fault mapping
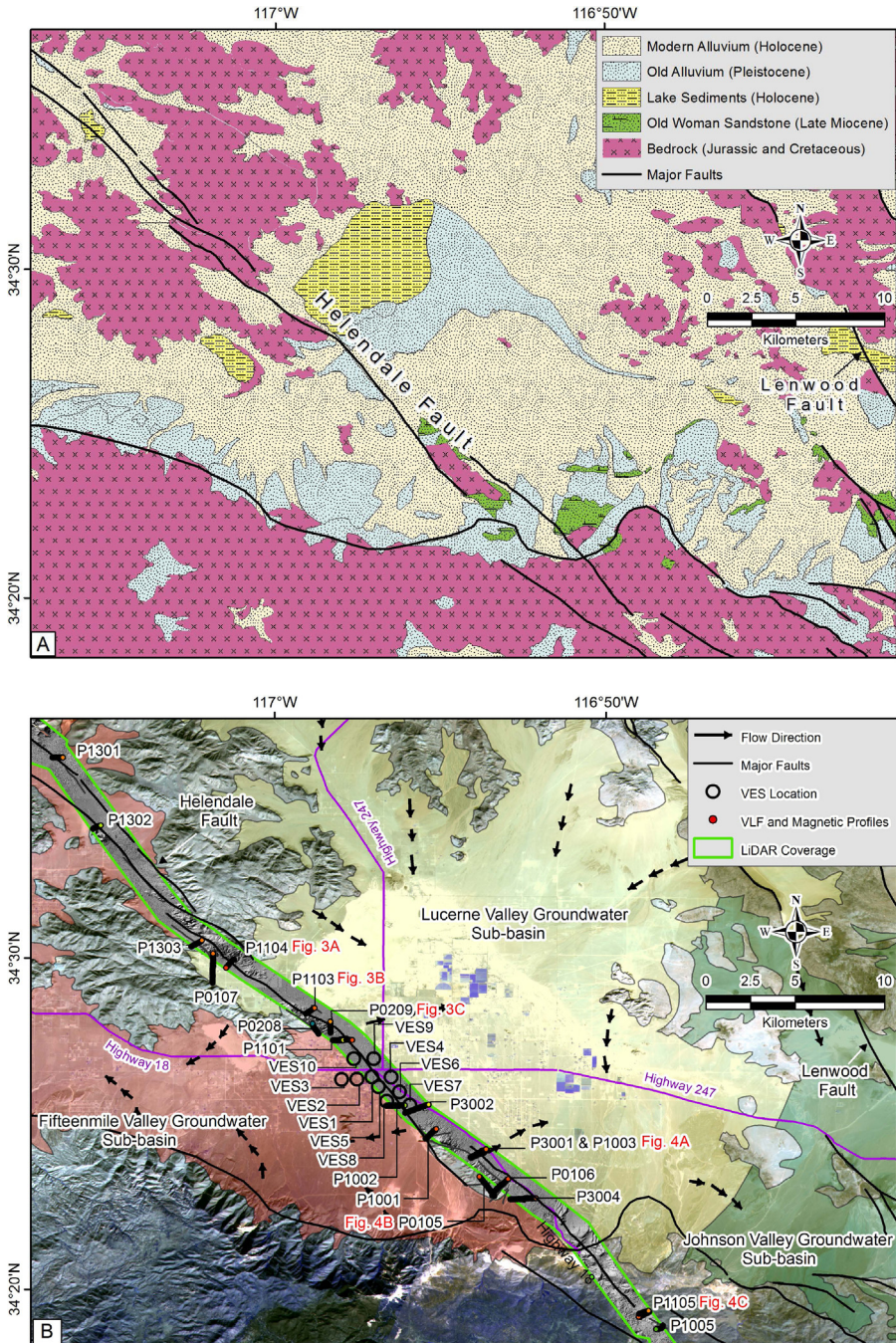
Fig. 2. (A) Simplified geologic map (modified from MWA, 2007) showing distribution of the major rock groups and bedrock ridges (subparallel to Helendale and Lenwood faults) that we infer to extend along their projected length at shallow depths beneath the overlying alluvium. (B) Location map for our VLF and magnetic profiles (thick black lines) and VES resistivity data (open circles). Also shown are (1) groundwater sub-basins (i.e., Lucerne Valley, Fifteenmile Valley, and Johnson Valley); and (2) groundwater flow direction within the sub-basins (Stamos and Predmore, 1995; ESA, 2004; MWA, 2005).

of all the faults is needed to define the appropriate location for conducting geophysical profiles. Second, we applied several geophysical techniques to verify the satellite-based distribution of faults using magnetic and electromagnetic measurements, and to examine the role of faults and basement uplifts in groundwater flow. Third, we collected groundwater samples from the study area to conduct isotopic analyses to search for isotopic provenances related to the distribution of faults and uplifts in the study area. Last, the collected geophysical and isotopic data were evaluated together with all other relevant hydrologic data (e.g., water levels) in a Geographic Information System (GIS) environment for a better identification of the spatial relationships and understanding of the significance of these relationships.

3.1. Remote sensing methods

The airborne Light Detection and Ranging (LiDAR; http://opentopo.sdsc.edu) laser (wavelength: 1047×10^{-9} m) emission and detection system produces detailed digital elevation images (spatial resolution: 1 m) of the surface while stripping away surface obscurers such as vegetation (Haugerud et al., 2003). The available LiDAR segments (12 segments) over and around the HF were used to identify small-scale features, such as subtle topographic changes and partially obscured fault features.

In areas were the LiDAR data are not available, the very high (panchromatic: 0.41 m, multispectral: 1.65 m) spatial resolution Google Earth GeoEye-1 images (www.geoeye.com) were used for examining smaller, less-regional features, including, but not limited to, fault splays. The LiDAR and GeoEye-1 data were used to better map the fault traces and splays of the HF for a better definition of the optimum locations for conducting geophysical surveys.

3.2. Geophysical methods

3.2.1. Very Low Frequency (VLF) profiles

The Very Low Frequency (VLF) radio receiver (IRIS T-VLF) was used to measure the distortion of the normally horizontal electromagnetic flux lines by local electrical conductors. The VLF uses the radio carrier waves of the submarine communications stations of the various navies of the world (Paterson and Ronka, 1971). The instrument records each frequency used, the tilt of the electromagnetic field (from the horizontal, given as a percentage), ellipticity in the vertical and horizontal planes, and signal strength.

We primarily used the VLF method (Paterson and Ronka, 1971) in the field to verify the presence of groundwater along the length of the HF and its splays. The VLF is ideal for this application, because it detects conductive water-saturated sub-vertical breccia zones in bedrock (Palacky et al., 1981). If the hypothesis that the dextral faults and intersecting fault splays in the LVGS and the FVGS are channeling groundwater is plausible, a significant conductive response in the VLF would be expected as the profile crosses the fault plane. However, the VLF instrument has several limitations. It responds strongly to massive sulfides, as well as to graphitic shear zones; however, the MRGB and the MGB are not known to contain these types of sulfide deposits and shear zones, so it is unlikely that interference would present itself in this form. It is also limited to detection within an approximately 90° fan of strikes (±45° from the radial azimuth to the transmitting station). To adjust for this, measurements were recorded using one of the three transmitting stations: Seattle, Washington (NLK at 24.8 kHz), which provided nearly ideal geometry for profiles acquired in an east or northeast direction; Lamour, North Dakota (NML at 25.2 kHz), for which only 2011 data was available, was used for the northwest-trending profiles; and Cutler, Maine (NAA at 24.0 kHz), was used as an alternative, since the receiver collects from two stations simultaneously. Data from the Cutler, Maine station was generally only used for north-trending profiles. The VLF method is limited to use during daylight hours, when the overhead ionosphere is well developed (Vallèe et al., 1992). It is also subject to sudden pulsations from the solar wind, which result in rapid deviations of the apparent tilt angle that may last for several minutes. In the event that such disturbances were encountered, data collection was paused or repeated to rule out this possible interference source.

Over the course of three summers (2009–2011), 19 profiles were performed in various locations across or near the HF (Fig. 2B). All profiles were acquired within the same time period (May–June) each year and some of these profiles were measured more than one time during the individual time periods.

These profiles were commonly acquired along the flanks of exposed ridgelines along the southern portion of the HF, the lower alluvial portions of the valley, and the canyons in the northern portion of the Lucerne Lake sub-basin. Some of these profiles were measured across suspected splays of the main fault, as opposed to crossing the HF itself. Several of these splays had been mapped previously, while others were identified using available geologic maps and remote-sensing datasets. Seven of these profiles will be detailed in the discussion section of this paper (Section 5).

3.2.2. Magnetic profiles

Magnetic profiles were used to define the subsurface postulated extension of the remote sensing-based (i.e., LiDAR, GeoEye-1) faults and fault splays and to help reveal the location of a fault plane where its location is not readily apparent or well known. Juxtaposition of rock units of varying magnetic susceptibilities usually shows as a magnetic anomaly as the profile crosses the fault plane. The Proton-Precession magnetometer (GeoMetrics G-816) was used to measure the absolute total magnetic field strength (in nano-Teslas [nT]) at the position of a sensor held on a staff approximately 2.5 m above the ground. The total magnetic field, location, and time of acquisition were recorded for every station. Because the Earth's magnetic field is subject to several time variations, of which the daily or diurnal variation is principle, a profile is usually preceded with a reading (and time) at an arbitrary local base station. The base station is then read again after completion of the profile. Since measurements along each of the profiles were acquired in less than an hour, the drift could be approximated as a simple linear function and readily corrected. Of the 19 VLF profiles conducted, 18 had magnetic data collected simultaneously.

3.2.3. Vertical Electrical Soundings (VES)

A Vertical Electrical Sounding (VES) is a type of resistivity measurement that measures electrical resistivity as a function of depth at a fixed point, assuming sub-horizontal layering (Telford et al., 1990). Changes in resistivity were used to identify changes in lithology and the location of the water table below the measurement point. Individual VES measurements were integrated to produce a geo-electric cross section from which the lithologic and hydrologic variations across a profile path were constructed.

The VES measurements taken in the field (using IRIS SYSCAL R2) were performed using a four-electrode expanding Schlumberger Array. In this array, the two potential electrodes (M and N) are kept fixed for three to five different expansions of the current electrodes (A and B). Because the current electrode spacing (A–B) is the primary control of the depth distribution of current lines (in addition to the resistivity layering structure), the AB or AB/2 distance is the reference for each reading. We used AB/2 spacings that increased from 1.0 m to 147 m in equally spaced intervals on a logarithmic scale, six spacings per decade. MN spacings were always 1/5 or less of the AB spacings. At the point where the measuring electrodes were expanded, another reading was taken without moving the current electrodes, providing data overlap. The first stage of treatment of the Schlumberger VES data was to make a smooth curve (on a log resistivity versus log of AB/2) either by adjusting segments up or down or by averaging the overlap points if the offset is small (<1%). Finally, an inversion routine was used to convert field resistivity versus AB/2, to interpreted resistivity versus depth. A total of 10 soundings were taken near a central location of the HF (Fig. 2B).

3.3. Isotopic methods

Twenty-two groundwater samples were collected (winter 2010) from shallow (depth: 40–70 m) production wells penetrating the Regional Aquifer and six samples were collected (spring 2011) from the springs in the foothills of the San Bernardino Mountains. The hydrogen and oxygen isotopic ratios were analyzed using a Picarro Cavity Ring-down Spectroscopy (CRDS) laser system (Lehmann et al., 2009) at ISOTECH Laboratories in Champaign, Illinois. Hydrogen and oxygen stable isotope ratios are reported using conventional delta (δ) notation, in units of per mil (‰) deviation relative to the Vienna Standard Mean Ocean Water (V-SMOW), whereby

$$\delta(‰) = [(R_{sample}/R_{standard}) - 1] \times 10^3 \tag{1}$$

and $R = {}^{2}H/{}^{1}H$, or ${}^{18}O/{}^{16}$ (Coplen, 1996). Reproducibility of δ values for δ D is ±1‰ and that of δ ${}^{18}O$ is ±0.2‰. The isotopic analyses can be used to investigate the source(s) of groundwater and to identify mixing trends between these sources (e.g., Clark and Fritz, 1997). In general, contrasts in these isotopic compositions across structural features such as uplifts and faults could be indicative of the role these features play as barriers to the lateral groundwater flow that tends to homogenize the groundwater composition on both sides of the fault.

3.4. Geographic Information System (GIS) analyses

Analysis of the collected data for this project involved the generation of a database for data integration, analysis, and visualization; this was made possible by using Arc Info GIS and Arc Spatial Database Engine (SDE). The generated database incorporates all relevant co-registered digital mosaics with a unified projection (World Geodetic System [WGS] 84) covering the southern Mojave Desert: (1) geologic map (scale 1:250,000); (2) LiDAR (swath width: 1.5 km; spatial resolution: 1 m) spanning the approximate length of the HF; (3) well data, provided by Mojave Water Agency, including one or more of the following parameters: well location, well name, well type (i.e., production, commercial, domestic, municipal), depth to water table, well elevation, and hydrogen and oxygen stable isotopic compositions; (4) IKONOS and eoEye-1 satellite scenes (spatial resolution 1–5 m); (5) California Alquist-Priolo (AP) Earthquake Fault Zone maps (scale 1:24,000) (Bryant and Hart, 2007); (6) VES soundings in the immediate vicinity of the HF; and (7) VLF and magnetic profiles acquired in tandem for dextral faults and intersecting fault splays in and near the HF.

4. Data and findings

4.1. VLF and magnetic data

VLF data can be examined directly on tilt-angle versus profile distance plots. Conductors are located where the tilt angle changes sign (zero crossover). Alternatively, simple filtering can be applied to remove short-wavelength features (e.g., single-station anomalies) and to shift the peaks by 90°. The four-point linear Fraser filter (Fraser, 1969) is widely used to accomplish this; it shifts the curve so that positive peaks are directly over the conductors. For a given sequence $(X_1, \ldots, X_n)$ of tilt angle measurements taken along the same profile at a regular station interval, the Fraser filtered value (F_1) was estimated as: $F_1 = (X_3 + X_4) - (X_1 + X_2)$ and plotted half way between positions of X_2 and X_3 measurements. Fraser (1969) pointed out that in optimal conditions a filtered peak of 5% may be significant, and that values can go as high as 100%. For this survey, we conservatively regarded Fraser-filtered peaks above 20% as significant, even though on some days the threshold could have been 10% or 15%, as verified by comparing profiles repeated at the same location on different dates.

Seven representative profiles are detailed in the discussion; five have magnetic data. Three of the profiles were acquired along the northern portion of the HF, and the remaining four were acquired along the southern portion of the fault. Fig. 3A–F shows the VLF and magnetic profiles at three locations (Fig. 2B: P1104, P1103, P0209) along the northern portion of the HF. A LiDAR swath or high-resolution GeoEye-1 imagery was used as a background image and faults were mapped locally (dashed lines) from these images. Several scenes also have the California AP as an added background; these zones outline buffer areas where movement along active faults has been measured since 1971 by the California Geological Survey (see www.consrv.ca.gov). The VLF responses shown in Fig. 3A–C, together with the magnetic measurements that were acquired simultaneously along the same profiles, were graphed in Fig. 3D–F. Similar displays (Fig. 4A–C) and response graphs (Fig. 4D–G) were generated for the VLF and magnetic profiles (Fig. 2B: P3001, P1003, P0105, and P1105) located along the southern portion of the HF in the more mountainous region southwest of Lucerne Valley.

Profile P1104 was performed in a box canyon, moving west to east (Fig. 3A and D). The modest VLF peak (Fraser Tilt [FT] 30%) aligns well with the main trace of the HF, which is well defined in the LiDAR dataset, and lies well within the mapped AP zone (light blue shaded areas outlined with thin black dotted lines). The magnetic response shows a change from a smooth, gentle gradient in the southwest
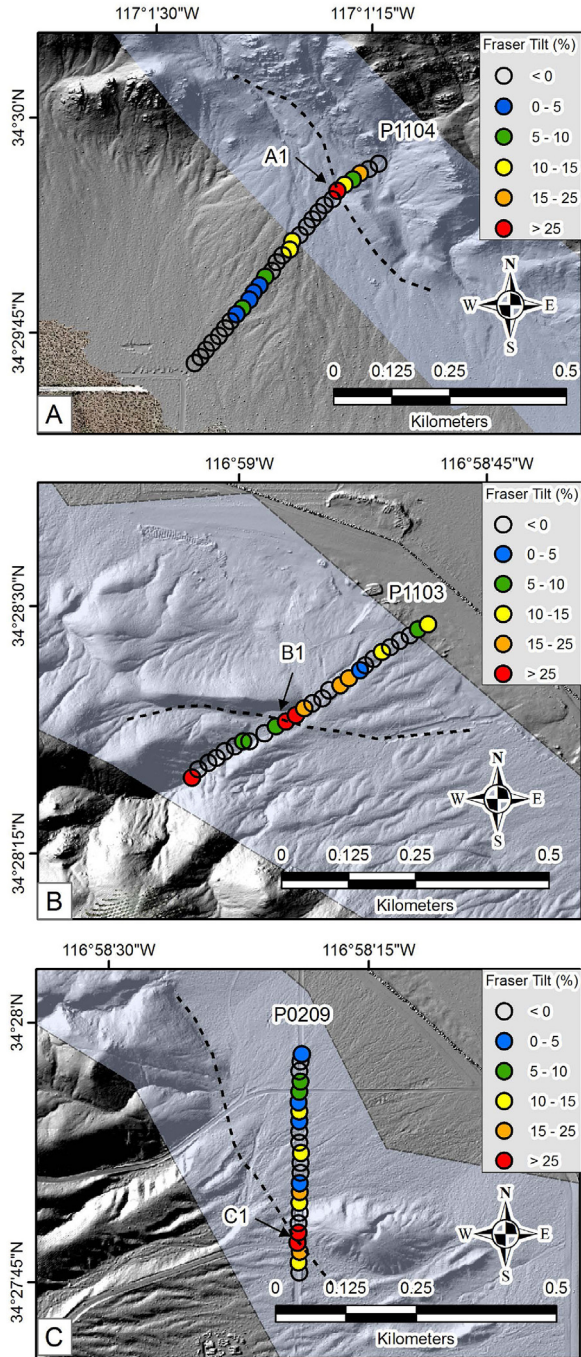
Fig. 3. Selected VLF and magnetic profiles and corresponding data plots for the northwest portion of the HF. (A–C) VLF responses (Fraser tilt ≥0%: colored circles; Fraser tilt <0%: hollow circles) over the fault locations (dashed black line) within California Alquist-Priolo (AP) zones (light blue area). (D–F) The data plots (red lines: Fraser tilt [%]; black lines: magnetic responses [nT]) for each of the measured profiles. Appreciable VLF and magnetic responses (marked by arrows) correspond to known (black dashed lines) fault locations in (A–C).
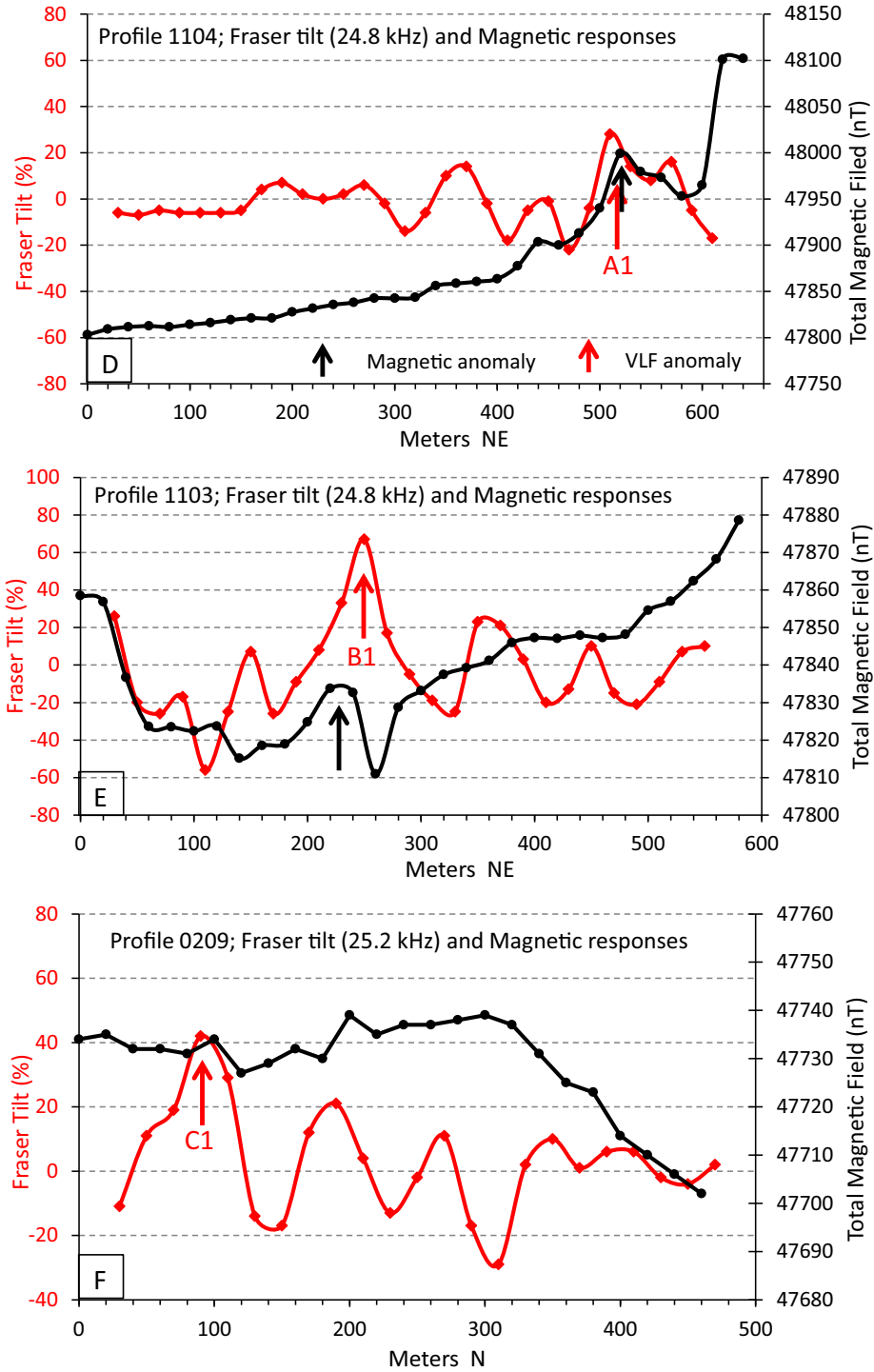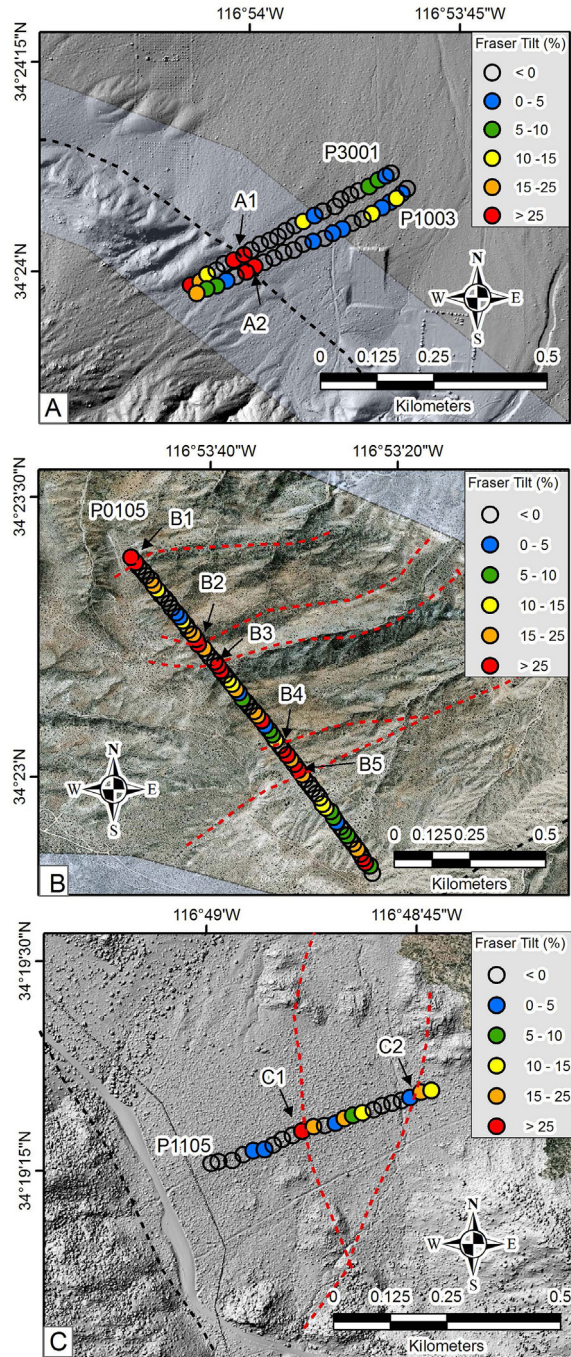
Fig. 3. (Continued.)

Fig. 4. Selected VLF and magnetic profiles and corresponding data plots for the southeast portion of the HF (black dashed line), fault splays (red dashed line) mapped from LiDAR and Geoeye-1 imagery, and California Alquist-Priolo (AP) zones (light blue area). (D–F) The data plots (red lines: Fraser tilt [%]; black lines: magnetic response [nT]) for each of the measured profiles. Appreciable responses (marked by arrows) correspond to known fault locations (black dashed lines) or LiDAR- and satellite-based inferred fault locations (red dashed lines) on (A–C).
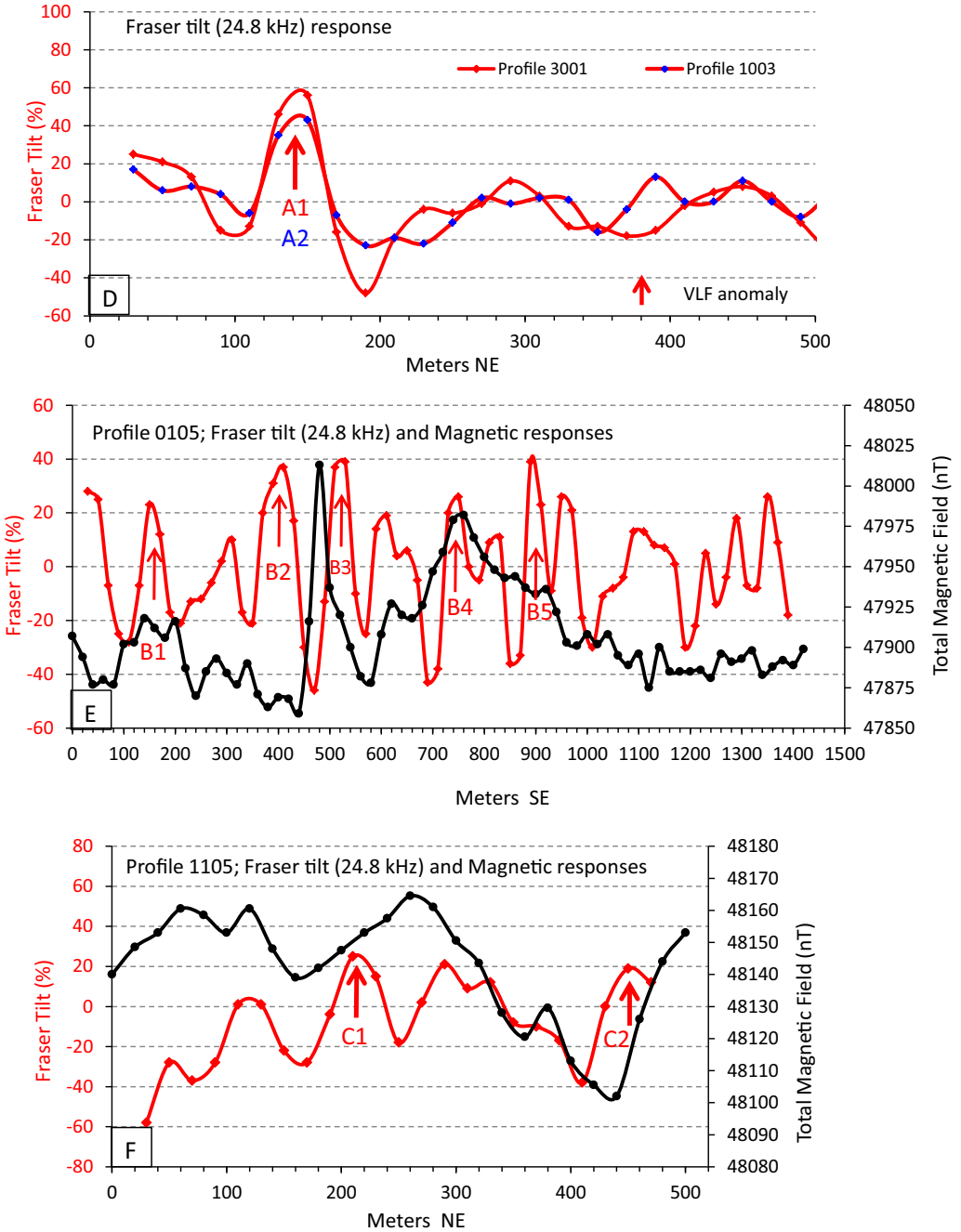
Fig. 4. (*Continued.*)

to steeper gradients and a local maximum at the location of the FT VLF maximum. This is an indication of the juxtaposition of two different basement lithologies and/or shallow basement to the northeast and deeper basement to the southwest. Profile P1103 (Fig. 3B and E) shows good responses with both magnetic and VLF methods. The strong VLF anomaly (FT 65%) aligns with a clear dipolar magnetic response. Both responses align well with a mapped fault that is shown on the LiDAR image and is also identified on geologic maps. This fault also lies well within the mapped AP zone for the HF. This fault is most likely a branch of the primary HF that "kinks" through the large ridge, with the main trace obscured to the east, or possibly still buried beneath the relatively shallow valley sediments. Another strong anomaly at the beginning of the profile (southwest end) aligns with a major fault, which is most likely the reason for the large depression seen in the LiDAR image. Profile P0209 (Fig. 3C and F) shows a strong VLF response (FT 45%) that aligns well with a mapped portion (AP zoning and local geologic maps) of the HF, which curves through the canyon in this area. The magnetic profile does not show any significant trend changes or anomalies at this position.

Fig. 4A–C shows four VLF profiles, two of which also have magnetic data. Profiles 3001 and 1003 (P3001, P1003; Fig. 4A and D) are repeat profiles, done each year in approximately the same location. P1003 was performed in summer of 2009, while P3001 was performed earlier in the summer of 2011 (after a wetter spring). P3001 shows a single, well-defined peak with a FT of 56% very near the fault plane, while P1003 shows a similar peak with a FT of 43%. Both peaks also align very well with the mapped AP zone for this area of the HF. The profile from 2011 showed a significantly higher response than that from 2009 (FT 13% higher). This is most likely due to the timing of the profile and the increased amount of groundwater still present in the fault plane when measured. Both profiles show high FT values at the start (southwest end), indicating another possible fault splay to the left and higher up the slope of this ridge.

Profile 0105 (P0105; Fig. 4B and E) runs parallel to the HF and crosses at high angles a series of suspected fault splays that intersect the HF itself. In each case, an appreciable peak (FT ≥ 20%) is seen as the profile crosses the fault traces, indicating the presence of shallow sub-vertical conductive sheets, most likely groundwater within high-angle fault splays. If these splays connect to the HF, they could possibly collect additional groundwater to add to that already channeled by the main fault. This magnetic profile shows much more variability than most of the other measured profiles. Bedrock is very shallow, and there are obvious lithologic variations and topographic effects along the profile that probably cause most of the observed abrupt magnetic changes. P1105 crosses two suspected splays (Fig. 4C: red dashed lines) of the HF (mapped as a black dashed line) in the far south. The fault traces here are fairly well defined, and two appreciable VLF peaks are observed as each fault trace is crossed, again indicating the presence of a shallow, conductive material. The magnetic profile for this transect is not diagnostic of faulting (Fig. 4F). Our VLF data are consistent with the interpretation that the HF is providing enhanced groundwater flow opportunities along strike.

4.2. VES data

The locations as well as the inversion results (number of layers, resistivity, thickness, depth and rms fit values) of the 10 VESs are shown in Fig. 5A. VESs 9, 4, 6, and 7 were aligned parallel and offset to the east of the fault; VESs 10, 1, 5, and 8 were located parallel to the west side of the fault. In addition, soundings 2 and 3 were positioned west of VES 1, thus creating a west-east geoelectric section (VESs 3, 2, 1, and 4) across the fault.

East of the fault, the four soundings show a strong similarity in curve types, each with two maxima. The northernmost sounding (VES 9) shows the first maximum is at the surface and becomes progressively deeper to the south. The intervening minimum and the second maximum also become progressively deeper; overall resistivities increase as the soundings progress south-southeast and up the alluvial fan to higher elevations. Each of these four soundings ends with a steeply declining branch, indicating that the conductive, saturated zone is being detected. This conductive zone is observed at progressively greater depths to the south-southeast. The two maxima are likely coarse-grained vadose zone sediments sandwiching a more conductive fine-grained unit.

A very different trend is observed west of the fault. In general, a much lower trend in resistivities is observed in each of the soundings when compared to similarly placed soundings east of the fault.
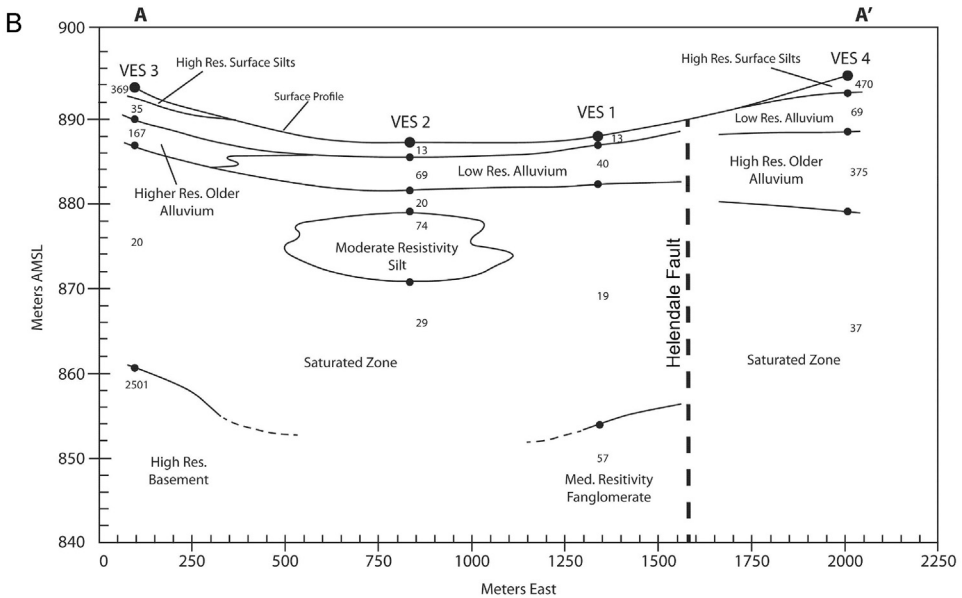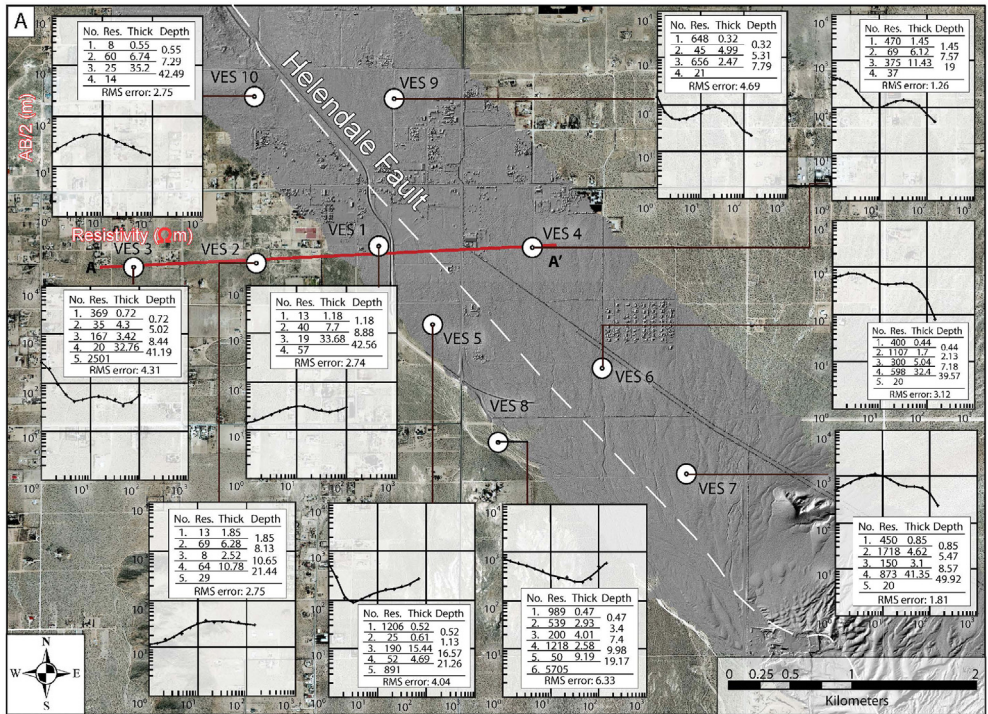
Fig. 5. (A) VES location, apparent resistivity, thickness, and distribution of saturated and unsaturated rock units in areas west (VESs 10, 3, 2, 1, 5, and 8) and east (VESs 9, 4, 6, and 7) of the HF (white dashed line). Also shown is the distribution of LiDAR (wavelength: 1047×10^{-9} m) data. (B) Geoelectric West-East trending cross-section A-A′ showing the VES (1–4) locations and apparent resistivity (Ω m), thickness (m a.m.s.l), and distribution of the saturated and unsaturated rock units. The top of the saturated zone represents the depth to water table. The vertical dashed line represents the inferred location of the HF.

They are similar only in that the resistivities rise, moving north to south up the alluvial fan surface. The right (deepest) branch of the log-log VES curves 1, 5, and 8 shows an increase in resistivity. This is in contrast to the case on the east side of the fault; the most plausible interpretation is that bedrock was encountered at fairly shallow depths. These sections were conducted along the strike of the topographic ridge to the southeast, and would appear to make a strong case for the continuation of that bedrock ridge in the subsurface all the way north to Lucerne Valley. If this is the case, then this bedrock ridge just to the west of the HF is likely what is blocking the eastward flow of groundwater across the fault. Flow is then only possible through a passage that is on the order of 1.5 km wide at the valley bottom, starting north of VES 1 and terminating against a ridge slightly north of VES 10 (this is the same ridge seen in Fig. 2A).

Soundings 3, 2, 1, and 4 (west-east row), show a clear change across the fault between soundings 1 and 4. They also show the low resistivity of the two central soundings (VES 2 and VES 1) where the surface sediments consisted of fine silts and clays, typical of the valley floor. The surface material at VES 3 was coarser, which typically causes higher resistivity, but the deeper resistivities were also low, as with soundings 1 and 2. The deepest segment of the curve for sounding 3 is a rising branch, possibly indicating another area of shallow bedrock. Another, much smaller, ridge is seen to the southeast of sounding 3 and may continue to the northwest beneath VES 3. It is reasonable to assume that this ridge, like the ridge that parallels the HF, continues northwest in the shallow subsurface before outcropping again to the northwest.

The geoelectric cross-section (Fig. 5B) along line A–A′ (Fig. 5A) shows that the vertical resistivity structure at VES 4 is different from that of VESs 1–3. West of the fault, the water table is interpreted at about 7–10 m depth, and a short distance east of the fault it is double that value. East of the fault, a thick, high-resistivity ($375\,\Omega$ m) unsaturated zone is present, whereas a much lower resistivity, probably reflecting finer-grained sediments, is observed west of the fault. Two of the VESs to the west appear to have reached high-resistivity basement rock at depths of about 40 m. This supports the hypothesis of a shallow bedrock sill joining the topographic ridges to the northwest and southeast.

Analysis of our resistivity data indicate the presence of high resistivities west of the fault at the right end of some of these VES curves, characteristic of shallow bedrock; east of the HF, the VES curves end at low values typical of aquifer units, not bedrock. These high resistivities occur along the strike of a prominent bedrock ridge, which runs parallel to the HF and dips below the surface along the valley floor. Further west of the fault, shallow resistivity is much lower and fits with mapped geologic units of young alluvium overlying older, higher-resistivity alluvium. Farther west still, another deep resistivity high is seen, again along strike of a bedrock ridge to the southeast. It is quite possible that these ridges are generally preventing groundwater from flowing east through the faulted zone, except across open "windows" or saddles between the shallow bedrock ridges that trend parallel to the fault.

4.3. Stable isotope data

Isotopic analyses (δD and δ^{18}O) were conducted on groundwater samples collected from productive wells and springs. The distribution of the well and spring samples is given in Fig. 6, and the isotopic analyses of these samples are presented in Table 1 and Fig. 7; well and spring samples are labeled "mwa" and "wmu" samples, respectively. Inspection of Table 1 and Figs. 6 and 7 show that many of the samples plot to the right of the global meteoric, which suggests that they were subjected to variable degrees of evaporation. Previous studies in the LVGS and surrounding area suggested that the aquifers in the investigated areas have been recharged in part in previous wet and cool climatic periods (Smith et al., 1992; Izbicki, 2004). The analyzed groundwater samples were classified into three groups based on their sampling location with respect to the HF: (1) Group I (mwa: 2, 14–16; wmu: 1, 2) were collected west of the fault from the FVGS; (2) Group II (mwa: 3, 4, 6–10, 17, 18, 20–24; wmu: 4) were sampled from the LVGS; and Group III (mwa: 1, 12, 13, 19; wmu: 3, 5, 6) were collected from locations proximal (<1.5 km) to the HF.

Group I samples (δD: −85.2‰ to −88.2‰, average: −86.8‰; δ^{18}O: −11.4‰ to −12.2‰, average: −11.8 ‰) plot along an evaporation line (Fig. 7; EVL) with a source whose composition (δD: −89‰; δ^{18}O −12.3‰) is given by the intersection of the evaporation and global meteoric lines. The inferred composition for the source is similar to that for groundwater (δD: −84 ‰) from wells recharged by
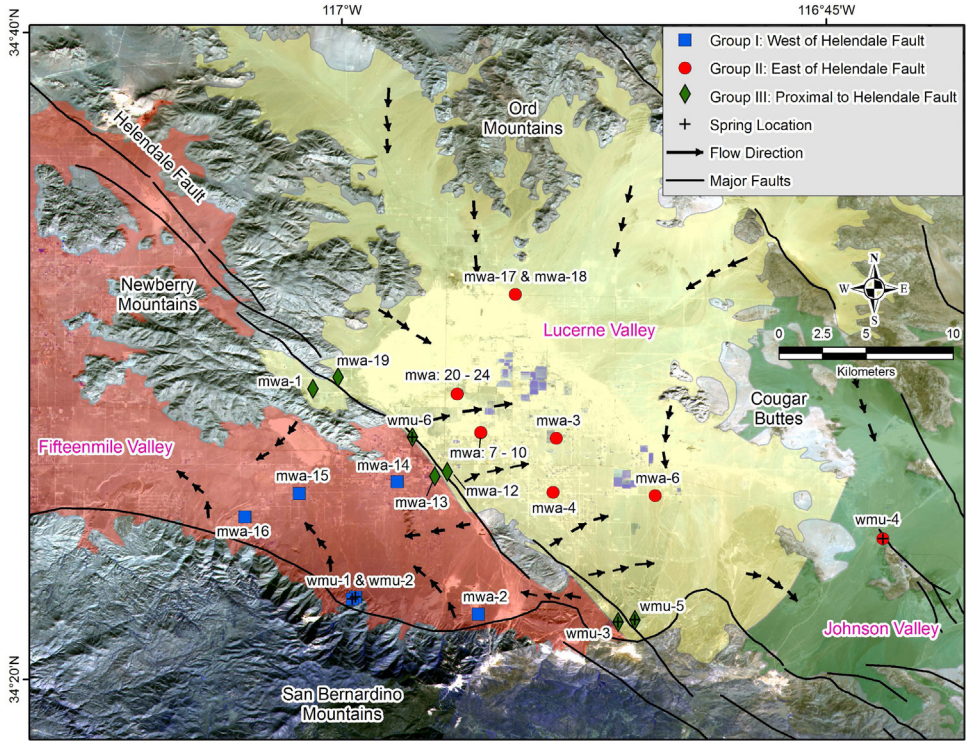
Fig. 6. Locations of wells (name designation: mwa) and springs (black cross; name designation: wmu) sampled for isotopic analyses (O, H) grouped into three main groups (I: West of HF [blue squares]; II: East of HF [red circles]; III: proximal to HF [green diamonds]). Also shown are (1) Groundwater sub-basins (i.e., Lucerne Valley, Fifteenmile Valley, and Johnson Valley); and (2) groundwater flow direction within the sub-basins (Stamos and Predmore, 1995; ESA, 2004; MWA, 2005).
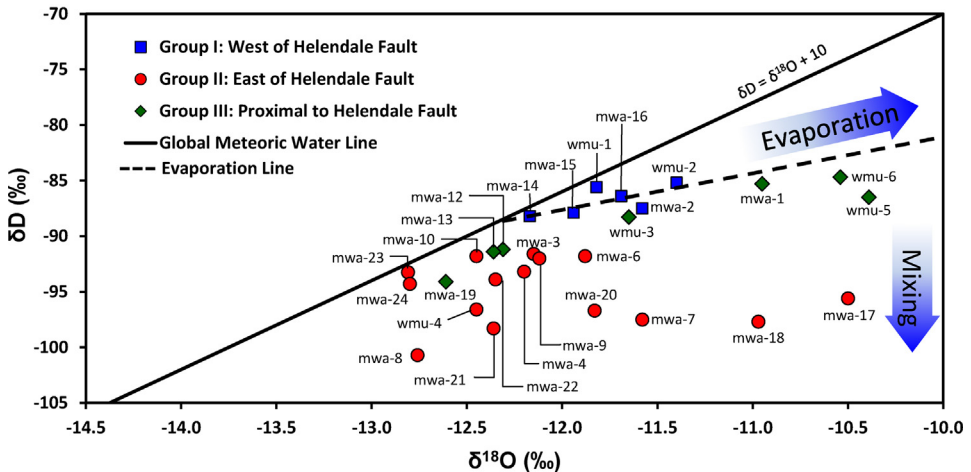

Fig. 7. Comparison between stable isotope ratios (hydrogen [δD] versus oxygen [δ^{18}O]) for groundwater samples from wells and springs west, east, and proximal to the HF. Also shown are the evaporation line for Group I samples, and its intersection (δD: −89‰; δ^{18}O: −12.3‰) with the Global Meteoric Line (δD = δ^{18}O + 10; Craig, 1961).

Table 1
Isotopic data for groundwater samples from wells and springs from the Fifteenmile Valley and Johnson Valley groundwater sub-basins.

Name	Groundwater sub-basin	Latitude (DD[a])	Longitude (DD)	Elevation (m)	Well description	Sample depth (m)	DTW[b] (m)	δD (‰)	δ¹⁸O (‰)
wmu-1	Fifteenmile Valley	34.3758	−116.9929	1356.1	Mountain Front Spring	N/A	0	−85.6	−11.8
wmu-2	Fifteenmile Valley	34.3747	−116.9945	1356.1	Mountain Front Spring	N/A	0	−85.2	−11.4
wmu-3	Lucerne Valley	34.3628	−116.8575	1398.7	Mountain Front Spring	N/A	0	−88.3	−11.7
wmu-4	Johnson Valley	34.4058	−116.7208	966.8	Valley Spring	N/A	0	−96.6	−12.5
wmu-5	Lucerne Valley	34.3641	−116.7488	1270.1	Mountain Front Spring	N/A	0	−86.5	−10.4
wmu-6	Fifteenmile Valley	34.4582	−116.9636	875.1	Valley Spring	N/A	0	−84.7	−10.5
mwa-1	Lucerne Valley	34.4830	−117.0150	916.5	Domestic Well	–	–	−85.3	−11.0
mwa-2	Fifteenmile Valley	34.3669	−116.9295	1263.4	Production Well	–	–	−87.5	−11.6
mwa-3	Lucerne Valley	34.4575	−116.8893	891.8	Production Well	–	–	−91.6	−12.2
mwa-4	Lucerne Valley	34.4298	−116.8910	925.7	Domestic Well	69	50.3	−93.2	−12.2
mwa-6	Lucerne Valley	34.4280	−116.8384	933.6	Domestic Well	–	–	−91.8	−11.9
mwa-7	Lucerne Valley	34.4605	−116.9283	876.9	Municipal Well	55	47.2	−97.5	−11.6
mwa-8	Lucerne Valley	34.4605	−116.9283	876.9	Municipal Well	55	46.3	−100.7	−12.8
mwa-9	Lucerne Valley	34.4605	−116.9283	876.9	Municipal Well	44	41.5	−92.0	−12.1
mwa-10	Lucerne Valley	34.4605	−116.9283	876.9	Municipal Well	55	46.6	−91.8	−12.5
mwa-12	Lucerne Valley	34.4402	−116.9456	904.3	Commercial Well	–	–	−91.2	−12.3
mwa-13	Lucerne Valley	34.4380	−116.9520	916.8	Domestic Well	–	–	−91.4	−12.4
mwa-14	Fifteenmile Valley	34.4352	−116.9714	909.8	Domestic Well	–	–	−88.2	−12.2
mwa-15	Fifteenmile Valley	34.4290	−117.0219	1033.3	Municipal Well	50.	25.3	−87.9	−11.9
mwa-16	Fifteenmile Valley	34.4170	−117.0500	877.8	Domestic Well	–	–	−86.4	−11.7
mwa-17	Lucerne Valley	34.5318	−116.9104	877.8	Municipal Well	55	46.3	−95.6	−10.5
mwa-18	Lucerne Valley	34.5318	−116.9104	884.5	Municipal Well	55	46.3	−97.7	−11.0
mwa-19	Lucerne Valley	34.4890	−117.0020	884.5	Domestic Well	–	–	−94.1	−12.6
mwa-20	Lucerne Valley	34.4805	−116.9405	869.9	Municipal Well	44	39.0	−96.7	−11.8
mwa-21	Lucerne Valley	34.4805	−116.9405	869.9	Municipal Well	44	39.3	−98.3	−12.4
mwa-22	Lucerne Valley	34.4805	−116.9405	869.9	Municipal Well	53	39.0	−93.9	−12.4
mwa-23	Lucerne Valley	34.4805	−116.9405	869.9	Municipal Well	53	39.3	−93.3	−12.8
mwa-24	Lucerne Valley	34.4805	−116.9405	869.9	Municipal Well	38	32.0	−94.3	−12.8

[a] DD – decimal degrees.

[b] DTW – depth to water table.

runoff from the higher altitudes of the San Bernardino and San Gabriel Mountains (Izbicki, 2004). Because two of these samples (wmu: 1 and 2) were collected from springs in the foothills of the San Bernardino Mountains, we suggest that the source of Group I samples is largely snowmelt from the mountains. This suggestion is consistent with earlier findings (USGS, 2004) indicating that the Regional Aquifer is being recharged by runoff and groundwater flow from the San Bernardino Mountains in the south. Irrespective of the source, the data clearly indicates that the water has undergone significant evaporation, which can take place during precipitation, in the unsaturated zone, or due to excessive use and "return flow" (Murad and Krishnamurthy, 2008).

Group II samples show a wide range of variation in their isotopic composition and are more depleted (δD: −91.6‰ to −100.7‰, average: −95.0‰; δ^{18}O: −10.5‰ to −12.8‰, average: −12.1‰) compared to Group I samples. It is likely that the LVGS is recharged largely from precipitation over the northern mountains (Ord, Rodman, and Stoddard mountains) (Blazevic et al., 2008) and that the groundwater flow is toward the southeast (Figs. 1 and 6). It is commonly thought that the HF acts as a barrier to lateral groundwater flow, which would prevent groundwater from the FVGS from mixing with that of the LVGS. This does not appear to be the case. Group II samples plot toward the Group I evaporation line (Fig. 7). These wells typically are east of the HF and fall along the east-southeast groundwater flow path in the LVGS. This indicates that groundwater mixing is occurring within the LVGS. The isotopic composition of Group III samples is consistent with an explanation that calls for various degrees of evaporation and mixing for Group I and II compositions. Samples collected from wells distant from the HF and proximal to their mountainous source areas (mwa: 17 and 18; Figs. 6 and 7) are the most separated from the evaporation line and thus could be the Group II samples least affected by mixing.

Carbon-14 ages (up to 43,000 year BP) reported for groundwater from the FVGS and the LVGS indicate that these aquifers were recharged at least in part in previous wet climatic periods (Izbicki and Michel, 2004). The depleted nature of Group II samples could be related to the fact that it is dominated by fossil groundwater; this suggestion is supported by the fact that the precipitation over the FVGS source areas (San Bernardino Mountains) far exceeds that over the LVGS source areas (Newberry and Ord mountains) (Izbicki, 2004; USGS, 2004). This could potentially lead to excessive flushing of the fossil water in the FVGS, and less flushing in the case of the LVGS.

Group III samples were taken from areas on either side of, and proximal to, the HF. In each case, the samples plot along, or close to but below, the evaporation line for Group I samples; their composition is slightly more depleted than Group I samples, yet more enriched than Group II samples (δD: −84.7‰ to −94.1‰, average: −88.8‰; δ^{18}O: −10.4‰ to −12.6‰; average: −11.5‰). This indicates that their composition is largely the same as that of Group I samples, the San Bernardino Mountain recharge waters; however, they show evidence for mixing with the Group II waters, the LVGS groundwater. This is to be expected if the HF is channeling Group I groundwater from the San Bernardino Mountains; limited mixing with Group II will occur proximal to the fault, and more extensive mixing will take place along the groundwater flow direction(s) within the LVGS.

Introduction of Group I groundwater in the LVGS is not only occurring by channeling groundwater along the HF, but possibly by groundwater flow across open "windows" or saddles between the shallow bedrock ridges that trend parallel to the fault. Two of these windows occur in the vicinity of wells mwa-13 and mwa-12, as well as at springs wmu-3 and wmu-5. In both cases, the bedrock ridge that cuts across the majority of the valley floor is unexposed at the surface. Since water levels west of the fault are relatively shallow, it is plausible that water is able to spill over the bedrock barrier in these locations, facilitating mixing between the aquifers. Regardless of which hypothesis is adopted, groundwater samples from the LVGS that have mixed isotopic compositions must have been derived, at least in part, from recharge waters in areas west of the fault because if an impermeable barrier were preventing lateral flow, these anomalous mixed composition values could not be explained.

If the HF is channeling Group I groundwater from the San Bernardino Mountains, one would expect that groundwater from areas proximal to the HF to have higher carbon-14 activities compared to those collected from areas distant from the fault. Inspection of reported carbon-14 activities expressed in percent modern carbon (pmc) (Izbicki and Michel, 2004) shows that is indeed the case; pmc values are high in samples collected from areas proximal to the HF (distance: 2–3 km; pmc: 69) and progressively decrease in values with increasing distance from the HF (distance: ∼15 km; pmc: 36) along postulated groundwater flow lines (Fig. 8). Similarly, high pmc values (pmc: 41–86) were reported from areas
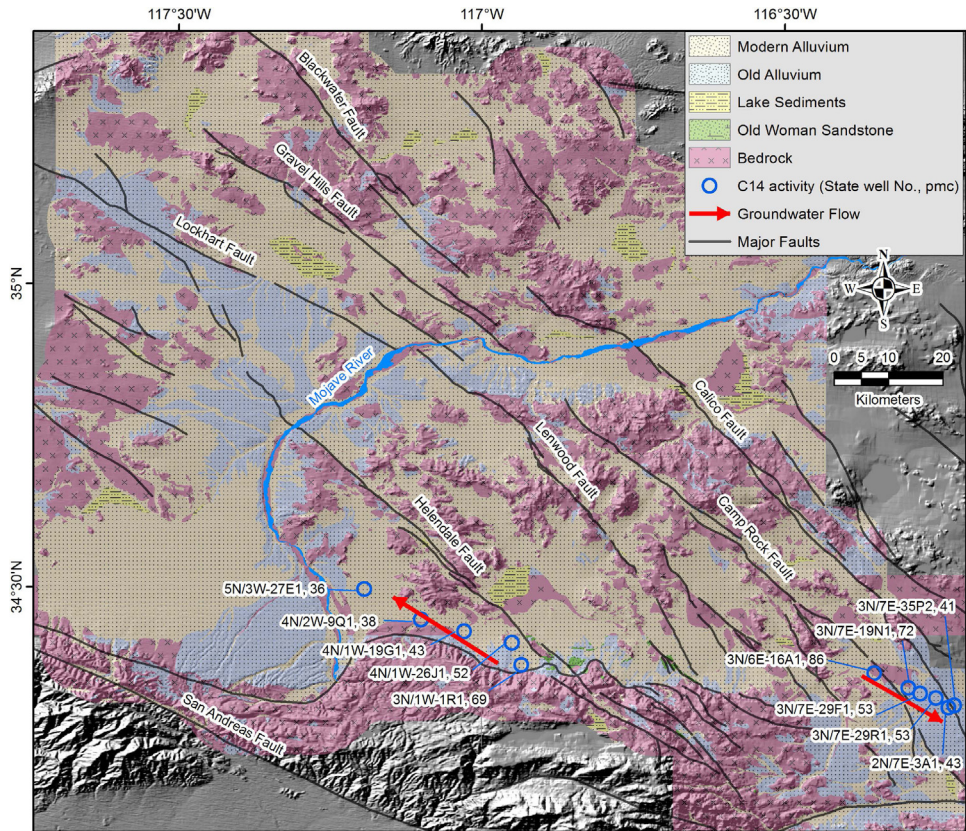
Fig. 8. Simplified geologic map (modified from MWA, 2007) with hillshade applied to accentuate topographic features showing the distribution of uplifted basement outcrops along and proximal to the major dextral faults in the Mojave Desert block. Also shown are sample locations, pmc values, and groundwater flow directions from Izbicki and Michel (2004).

proximal and downgradient from the Camp Rock Fault (Fig. 8). One would also expect to detect tritium downgradient from the HF if it is channeling Group I groundwater from the San Bernardino Mountains. Tritium was detected in observation wells tapping the Regional Aquifer and underlying deposits downgradient from the HF; it was also detected downgradient from the Camp Rock Fault (Izbicki and Michel, 2004).

5. Results and regional implications

Our data (VLF, VES, O, H isotopic composition) and reported pmc values (Izbicki and Michel, 2004) are consistent with the interpretation that the HF is providing enhanced groundwater flow opportunities along strike, and channeling groundwater from the higher-elevation areas in the south to the lowland areas in the central and northern portions of the MRGB and MGB. The VLF data shows that the majority of locations along the HF are conductive, indicating that the fault plane contains groundwater even at higher elevations on the southern ridges.

Our groundwater samples show evidence for varying degrees of evaporation and mixing. Samples taken in areas to the east of the HF (Group II), especially those from wells along the east-southeast groundwater flow path in the LVGS groundwater and those that were sampled proximal to the HF (Group III), show limited mixing and more extensive mixing along groundwater flow path within the LVGS. One way for such mixing to occur is for the fault to channel groundwater through its fracture

planes, many of which are observed within the bedrock ridges. If the HF acted as an impermeable barrier preventing lateral flow, these mixed-composition values from the LVGS could not be explained, since these samples must have been derived, at least in part, from recharge waters in areas west of the fault.

If the HF is not a barrier for lateral groundwater flow, then what is causing the observed change in water level across the fault? West of the fault, groundwater is found an average of 5–10 m below surface level, while to the east of the fault, groundwater depth averages 45 m below surface level (Smith and Pimentel, 1998; Stamos et al., 2003). Our geophysical data (VES) suggest that the groundwater drop across the HF can be at least partially attributed to the shallow bedrock ridges that restrict or impede the groundwater from flowing east across the fault. The presence of basement uplifts running parallel and proximal to the HF could be also inferred from the trail of uplifted basement outcrops that are parallel to, and bound by, the fault traces (Figs. 1 and 8).

Our findings for the HF might be relevant to many of the other major dextral faults within the Mojave Desert block. As is the case with the HF, the Lenwood, Camp Rock, Calico, and Granite mountains and Johnson Valley faults are decorated by uplifted basement outcrops along the majority of their lengths (Fig. 8). A strong relationship between topography and the strain domains has been observed within the Mojave Desert block. Many of the elevated areas, previously referred to as uplifts, in the Mojave Desert block are experiencing oblique shear resulting from dextral strike-slip shear and shortening (Dokka and Macaluso, 2001).

This study highlights the potential for identifying similar fault zones throughout the Mojave Desert region, since it is likely that these faults, especially those with exposed bedrock ridges trending along their length, will exhibit similar behavior; they channel groundwater along their length from source areas in the highlands to populated areas in the lowlands. From a groundwater supply standpoint, this is important because it indicates additional resources may be available for the dry, low-precipitation areas, which are increasing in population each year. Caution should be exercised in generalizing our findings. Studies similar to the ones advanced here should investigate whether the faults that experience a large throw and generate a wide gouge zone, like the San Andreas Fault, are channeling groundwater along their strike like the HF and in the same time acting as barriers for lateral groundwater flow as originally perceived.

Conflict of interest

None.

Acknowledgements

References

Barton, C.A., Zoback, M.D., Moos, D., 1995. Fluid-flow along potentially active faults in crystalline rock. Geology 23, 683–686.
Blazevic, M., Laton, W.R., Foster, J., 2008. Geologic Insight to Lucerne Valley Groundwater Basin. California State University, Fullerton.
Bense, V.F., Person, M.A., 2006. Faults as conduit-barrier systems to fluid flow in siliciclastic sedimentary aquifers. Water Resour. Res. 42, W05421, http://dx.doi.org/10.1029/2005WR004480.
Bense, V.F., Van Balen, R.T., DeVries, J.J., 2003. The impact of faults on the hydrogeological conditions in the Roer Valley Rift System: an overview. Neth. J. Geosci. 82 (1), 41–54.
Bryant, W., Hart, E., 2007. Fault-rupture Hazard Zones in California: Alquist-Priolo Earthquake Fault Zoning Act with Index to Earthquake Fault Zones Maps. Special publication no. 42, California Geological Survey., pp. 1–42.
Caine, J.S., Evans, J.P., Forster, C.B., 1996. Fault zone architecture and permeability structure. Geology 24, 1025–1028.
Caine, J.S., Minor, S.A., 2009. Structural and geochemical characteristics of faulted sediments and inferences on the role of water in deformation, Rio Grande Rift New Mexico. Geol. Soc. Am. Bull. 121 (9–10), 1325–1340.

Celico, F., Petrella, E., Celico, P., 2006. Hydrogeological behaviour of some fault zones in a carbonate aquifer of Southern Italy: an experimentally based model. Terra Nova 18, 308–313.

Clark, I.D., Fritz, P., 1997. Environmental Isotopes In Hydrogeology. CRC Press/Lewis Publishers, Boca Raton, FL.

Coplen, T.P., 1996. New guidelines for reporting stable hydrogen, carbon and oxygen isotope-ratio data. Geochim. Cosmochim. Acta 60, 3359–3360.

Craig, H., 1961. Isotopic variations in meteoric waters. Science 133, 1702–1703.

Dewandel, B., Lachassagne, P., Wyns, R., Maréchal, J.C., Krishnamurthy, N.S., 2006. A generalized hydrogeological conceptual model of granite aquifers controlled by single or multiphase weathering. J. Hydrol. 330, 260–284.

Dokka, R., 1983. Displacements on late Cenozoic strike-slip faults of the Central Mojave Desert, California. Geology 11, 305–308.

Dokka, R.K., 1986. Patterns and modes of early Miocene extension of the central Mojave Desert California. In: Mayer, L. (Ed.), Extensional Tectonics of the Southwestern United States, vol. 208. Geological Society of America Special Paper, pp. 75–95.

Dokka, R., Travis, C., 1990. Late Cenozoic strike-slip faulting in the Mojave Desert, California. Tectonics 9, 311–340.

Dokka, R.K., Henry, D.J., Ross, T.M., Baksi, A.K., Lambert, J., Travis, C.J., Jones, S.M., Jacobson, C.E., McCurry, M.M., Woodburne, M.O., Ford, J.P., 1991. Aspects of the Mesozoic and Cenozoic geologic evolution of the Mojave Desert. In: Walawender, M.J., Hanan, B.B. (Eds.), Geological Excursions in Southern California and Mexico. Geological Society of America Annual Meeting Field Trip Guidebook, San Diego, California.

Dokka, R., Macaluso, Y., 2001. Topographic effects of the Eastern California Shear Zone in the Mojave Desert. J. Geophys. Res. 106, 20644–30625.

ESA (Environmental Science Associates), 2004. Mojave Water Agency 2004 Regional Water Management Plan, SCH#: 2003101119, Program Environmental Impact Report.

Faulkner, D.R., Jackson, C.A.L., Lunn, R.J., Schlische, R.W., Shipton, Z.K., Wibberley, C.A.J., Withjack, M.O., 2010. A review of recent developments concerning the structure, mechanics and fluid properties of fault zones. J. Struct. Geol. 32, 1557–1575.

Fraser, D.C., 1969. Contouring of VLF-EM data. Geophysics, 34958–34967.

Garfunkel, Z., 1974. Model for the late Cenozoic tectonic history of the Mojave Desert, California and for its relation to adjacent areas. Geol. Soc. Am. Bull. 85, 1931–1944.

GSI (Geothermal Surveys, Inc.), 2000. Results of Detailed Gravimetric Investigation, Yucca Mesa Area, San Bernardino County, California. Prepared for High Desert Water District. June 12, 2000.

Gudmundsson, A., 2001. Fluid overpressure and flow in fault zones: field measurements and models. Tectonophysics 336, 183–197.

Haugerud, R., Harding, D., Johnson, S., Harless, J., Weaver, C., 2003. High-Resolution Lidar Topography of the Puget Lowland, 13. GSA Today, Washington, pp. 4–10.

Izbicki, J., 2004. Source and Movement of Ground Water in the Western Part of the Mojave Desert, Southern California, USA. USGS Water-Resources Investigations Report 03-4313.

Izbicki, J., Michel, T., 2004. Movement and Age of Ground Water in the Western Part of the Mojave Desert, Southern California, USA. USGS Water-Resources Investigations Report 03-4314.

Knipe, R., 1993. The influence of fault zone processes and diagenesis on fluid flow. In: Horbury, A., Robinson, A. (Eds.), Diagenesis and Basin Development, 36. American Association of Petroleum Geologists Studies in Geology, pp. 135–151.

Lehmann, K.K., Berden, G., Engeln, R., 2009. An introduction to cavity ring-down spectroscopy. In: Berden, G., Engeln, R. (Eds.), Cavity Ring-Down Spectrometry Techniques and Applications. John Wiley & Sons Ltd., United Kingdom, pp. 1–26.

Lewis, R.E., 1972. Ground-water Resources of the Yucca Valley-Joshua Tree Area, San Bernardino County, California. USGS Open-File Report 72-234.

Londquist, C.J., Martin, P., 1991. Geohydrology and groundwater flow simulation of the Surprise Spring Basin Aquifer System, San Bernardino County, CA. USGS Water Resources Investigation Report 89-4099.

Lunn, R.J., Wilson, J.P., Shipton, Z.K., Moir, H., 2008. Simulating brittle fault growth from linkage of preexisting structures. J. Geophys. Res.–Solid Earth 113, B07403.

Meisling, K.E., (PhD thesis) 1984. Neotectonics of the North Frontal Fault System, of the San Bernardino Mountains, Southern California: Cajon Pass to Lucern Valley. California Institute of Technology.

MWA (Mojave Water Agency), 2005. Este Hydrologic Atlas.

MWA (Mojave Water Agency), 2007. Geologic map for a portion of the Eastern Mojave Desert, San Bernardino County, CA, 1: 250,000.

Murad, A.A., Krishnamurthy, R.V., 2008. Factors controlling stable oxygen, hydrogen and carbon isotope ratios in regional groundwater of the eastern United Arab Emirates (UAE). Hydrol. Process. 22, 1922–1931.

Palacky, G.J., Ritsema, I.L., Jong, S.J., 1981. Electromagnetic prospecting for groundwater in Precambrian Terrains in the Republic of Upper Volta. Geophys. Prospect. 29, 932–955.

Paterson, N.R., Ronka, V., 1971. Five years of survey with the very low frequency electromagnetic method. Geoexploration 9, 7–26.

Smith, G., Pimentel, I., 1998. Regional Water Table (1998) and Groundwater-Level Changes in the Mojave River and the Morongo Ground-Water Basins, San Bernardino County, California. USGS Water-Resources Investigation Report 00-4090.

Smith, G., Friedman, I., Gleason, J.D., Warden, A., 1992. Stable isotope composition of waters in southeastern California: 2. Groundwaters and their relation to modern precipitation. J. Geophys. Res. 97, 5813–5823.

Stamos, C.L., Predmore, S.K., 1995. Data and water-table map of the Mojave River ground-water basin, San Bernardino County, California, November 1992: U.S. Geological Survey Water-Resources Investigations Report 95-4148, scale 1:125,000.

Stamos, C., Martin, P., Nishikawa, T., Cox, B., 2001. Simulation of Ground-Water Flow in the Mojave River Basin, California. USGS Water-Resources Investigations Report 01-4002 Version 3.

Stamos, C., Cox, B., Izbicki, J., Mendez, G., 2003. Geologic Setting, Geohydrology and Ground-Water Quality near the Helendale Fault in the Mojave River Basin, San Bernardino Country, California. USGS Water-Resources Investigations Report 03-4069.

Sultan, M., Wagdy, A., Manocha, N., Sauck, W., Gelil, A., Youssef, A.F., Becker, R., El Alfy, Z., Jones, C., 2007. An integrated approach for identifying aquifers in transcurrent fault systems: the Najd shear system of the Arabian Nubian shield. J. Hydrol. 349, 475–488.

Telford, W.M., Geldart, L.P., Sheriff, R.E., 1990. Applied Geophysics, second edition. Cambridge University Press.
Trayler, C.R., Koczot, K.M., 1995. Regional Water Table (1994) and Water-Level Changes in the Morongo Basin, San Bernardino County, California. USGS Water-Resources Investigations Report 5-4209.
USGS (United States Geological Survey), 2004. Precipitation History of the Mojave Desert Region, 1893–2001. U.S. Department of the Interior, USGS Fact Sheet 117-03.
Vallèe, M., Chouteau, M., Palacky, G.J., 1992. Effect of temporal and spatial variations of the primary signal on VLF total-field surveys. Geophysics 57, 97–105.